# ICEF2024-140686

# Effects of Exhaust Gas Recirculation on Laminar Burning Velocity and Flame Structure of Hydrogen/Air Flames

# Ahmed Baraina, Berk Can Duvab and Elisa Toulsona

<sup>a</sup> Alternative Fuels and Combustion Laboratory, Michigan State University, East Lansing, MI, USA box Rolls Royce North America, Reston, VA

### **ABSTRACT**

Engines have been a crucial element in powering our world since their invention. New decarbonization technologies are needed and hydrogen fuel, often referred to as the fuel of the future, has gained significant interest in this regard. The relatively high flame temperature of hydrogen fuel is associated with higher NOx emissions, and exhaust gas recirculation (EGR) can be used to address this. However, exhaust gas recirculation changes the reactivity and the laminar burning velocity of the mixture, which plays a significant role in flame stability and fuel burning rates. Hence, investigating the effect of EGR on laminar burning velocity is crucial for efficient hydrogen engines. Laminar burning velocity measurements were performed by observing the outwardly propagating flames in a constant volume combustion vessel. Measurements were taken at 2 bar, 373 K, equivalence ratios of 0.7 and 1.0 and dilution ratios of 0% to 50%. Chemical kinetic simulations were combined with the experimental measurements to quantify the effects of EGR (35% H<sub>2</sub>O+65%N<sub>2</sub>) on the laminar burning velocity and Markstein length. Results regarding Lewis number, flame thickness, and expansion ratio across the flame showed that adding higher EGR dilution can change flame stability and reduce cellularity of the hydrogen flames.

Keywords: hydrogen fuel, laminar burning velocity, EGR, flame instability, Markstein length.

# **NOMENCLATURE**

α	thermal diffusivity
β	number of H <sub>2</sub> O moles in the reactants
γ	specific heat ratio
δ	flame thickness
ξ	mixture strength
κ	stretch rate
$\rho_{\mathrm{u}}$	unburned gas density
$\rho_{b}$	burned gas density
σ	density ratio through the flame surface
φ	equivalence ratio

Α	flame surface area				
Ср	specific heat at constant pressure				
CPM	constant pressure method				
CVM	constant volume method				
E	activation energy				
K	thermal conductivity				
$L_{b}$	Markstein length				
$Le_E$	excess-reactant Lewis number				
$Le_D$	deficient-reactant Lewis number				
Le <sub>eff</sub>	effective Lewis number				
Le*	critical Lewis number				
P	pressure				
$R_f$	flame radius				
$R_u$	universal gas constant				
$S_{b}$	burned gas flame speed				
T <sub>0</sub>	inner layer temperature				
$S_{b}^{\circ}$	unstretched burned gas flame speed				
t	time				
$S_u^{\circ}$	laminar burning velocity				
Stoic	stoichiometric mixture condition				
$X_{dilution}$	dilution ratio, by volume				
Ze	Zeldovish number				
Z	number of N <sub>2</sub> moles in the reactants				
$(A/_F)_{\text{stoic}}$	stoichiometric air to fuel ratio				
EGR	exhaust gas recirculation				
H2-ICE	hydrogen internal combustion engine				
ICE	internal combustion engine				
LC	linear stretch model based on curvature				
MW	molecular weight				
NOx	nitrogen oxides				
Th 1					

### 1. INTRODUCTION

Ppmvd

For decades, the internal combustion engine (ICE) has been a reliable source of power for the world. Its compactness and flexibility have significantly increased its versatility across

parts per million per volume dry

applications that include transportation, aviation, and power generation. The growing reliance on internal combustion engines has led to increased energy demand, resulting in a dramatic rise in fossil fuel consumption and emissions in recent years. For example, in 2022, the transportation sector was responsible for 67% of the total petroleum consumption in the United States and gasoline accounts for the largest share, with approximately 369 million gallons of motor gasoline consumed per day [1]. Emissions from this petroleum fuel usage continue to serve as strong motivations for the development of cleaner and more efficient combustion systems. Therefore, carbonnatural fuels are desirable to mitigate the carbon footprint and emissions of ICEs.

In addition to its carbon-free combustion emissions, hydrogen also has the potential to be generated through electrolysis, powered by renewable wind/solar systems, and then be stored to serve as a backup system to solve the system intermittency issues [2]. Thermal efficiency of the H2-ICE is usually higher than their fossil-fueled counterparts due to the higher flame speeds and the more concentrated heat release near top dead center [3]. Since hydrogen has an extended flammability limit and low ignition energy, it is well suited for internal combustion engine applications, especially with the currently-sought ultra-lean burn techniques.

Other applications of hydrogen include mixing it with other renewable fuels, like ammonia [4]. Ammonia has a very high ignition energy [5,6] and is hindered by its slow flame speed, which can be addressed by mixing it with hydrogen to maintain carbon-free operation while achieving engine-required combustion characteristics. Several studies were conducted to investigate the performance of hydrogen fuel blends internal combustion engines [4,7–10] Although hydrogen addition improved the combustion process, mixing and storage of multiple fuels increased the system complexity [11].

H2-ICEs are associated with higher NOx emissions due to the elevated combustion temperatures [12]. Exhaust Gas Recirculation (EGR) has proven a reliable technique to reduce NOx emissions by lowering the combustion temperature [12–14]. However, the presence of EGR changes the thermodiffusive properties, the kinetics and the reactivity of the mixture and these effects can be investigated by measuring the laminar burning velocity ( $S_u^{\circ}$ ) of the diluted mixtures. Laminar burning velocity is a fundamental parameter in premixed combustion and a characteristic of the fuel performance. The laminar burning velocity affects ICEs emissions, burning rates, flame stability, misfire, knock, and engine performance.  $S_u^{\circ}$  data can also be used in the development of safety standards for production, transportation, and storage of hydrogen. Turbulent combustion simulations and the development and validation of chemical kinetics models also rely on the measured  $S_u^{\circ}$  data.

Rrustemi et al. [15] used one dimensional (1-D) Chemical kinetics to derive correlations of laminar burning velocity of hydrogen flames diluted with water at 10 to 70 bar, 400 to 800 K and equivalence ratios of 0.3 to 1.0. Their correlations were derived for water dilution ratios up to 20% and they captured

the temperature and pressure dependence in their correlations at engine conditions, while the 1-D simulation did not account for the flame cellularity associated with these conditions. Verhelst et al. [16] studied the effect of EGR on the laminar burning velocity of hydrogen fuel at pressures up to 10 bar and equivalence ratios of 0.3 to 1.0. Laminar burning velocity was extracted only during smooth flame propagation at 1 bar and an unstable flame speed was calculated at a fixed flame radius of 10 mm, which was used as an indication of the burning rate at higher pressures and leaner mixtures. Kwon and Faeth [17] measured the laminar burning velocity and Markstein length of diluted hydrogen/oxygen mixtures at pressures of 0.3 to 3.0 bar and equivalence ratios up to 4.5 at normal temperature. Helium, argon, and nitrogen were used to change the reactant thermodiffusive properties and combustion temperature to study the of positive stretch effect, due to flame curvature and flow strain, on the flame speed. In addition, chemical kinetic modeling was performed and flame instabilities were investigated.

Duva and Toulson [14] investigated the dilution effect of actual EGR on the flame speed of hydrogen/air mixtures at 1 bar for temperatures of 373 K to 473 K, and at 2 bar at 473 K at an equivalence ratio of 0.7. A reduction of flame speed and Markstein length was observed with increasing dilution ratios. Furthermore, correlations of flame speed and Markstein length were derived for the measured pressure and temperature ranges. Similar results were obtained by Barain and Toulson [18] for stoichiometric hydrogen-air mixtures at 1 bar and EGR ratios up to 50 %. Lamoureux et al. [19] also measured the flame speed of hydrogen-air mixture diluted with a mixture of (40% helium+60 % carbon dioxide) at different dilution ratios.

In the majority of the previous studies, diluents other than the actual exhaust products of hydrogen/air combustion were used, so further studies of the effects of actual EGR on flame stability are needed. Diluents like helium and argon are inert and they do not reflect the real EGR properties and this will change the thermal properties, particularly thermal conductivity and specific heat of the mixture [20]. In addition, inert gases have different molar mass than actual EGR and this affects the flame propagation [21]. Components of EGR can participate and interact in combustion pathways and this will affect the flame reactivity and kinetics [14,18]. Hence, diluting the mixture with EGR that is composed of gases that exist in the exhaust of the H2-ICE is more applicable for practical engine operation.

The focus of the current study is the effect of dilution on hydrogen-air flames using EGR with a composition similar to the actual composition of the exhaust gas of stoichiometric hydrogen combustion, 35% H<sub>2</sub>O + 65% N<sub>2</sub> by volume. This paper presents the experimental and simulation results of the effect of EGR dilution on hydrogen/air laminar burning velocity. The measurements were conducted using a cylindrical constant volume vessel at an initial pressure of 2 bar, initial temperature of 373 K, equivalence ratios ( $\phi$ ) of 0.7 and 1.0, and up to 50%, by volume, EGR. The changes in the laminar burning velocity and the flame response to stretch with dilution were investigated and the Markstein length was calculated for

the tested mixtures, as a measure of the flame-stretch interaction. The flame thickness, expansion ratio and effective Lewis number were calculated at different dilution ratios to further investigate the effect of EGR on flame instabilities. Experimental measurements were compared against chemical kinetic modeling results, and NOx formation was predicted from the chemical kinetic mechanism [22].

# 2. MATERIALS AND METHODS 2.1 Experimental system

The high flammability limits of hydrogen fuel enable ultralean premixed combustion for NOx control [7]. However, the slower flame speeds of the diluted mixture can affect the engine performance, in terms of combustion stability and emissions. Hence, understanding the dilution effect on hydrogen flame propagation speeds and flame stability is essential for the development of efficient H2-ICE. A constant volume combustion vessel has been shown to be a reliable technique for measuring the laminar burning velocity [5,18,23,24]. Here, the rate of propagation of spherically expanding premixed flames, based on the direct detection of the flame edge by high-speed imaging, is used to derive the laminar burning velocity,  $S_u$ . The ability to control initial pressure, initial temperature as well as the well-defined and uniform flame stretch have favored the constant volume combustion chamber over other measurement techniques [25]. Moreover, the flame propagation inside the constant volume chamber, where the premixed mixture is ignited by two electrodes, is similar to real-engine homogeneous mixture ignition. Laminar burning velocity data can be extracted either during the early flame propagation, when the flame propagation is nearly isobaric, the constant pressure method (CPM) [5,6,18,25], or during increasing vessel pressure, the constant volume method (CVM) [26,27]. The CPM has the advantage of detecting flame instabilities, rather than solely depending on the pressure measurement as in the case of the CVM. Hence, the CPM was adopted in the current study, due to the propensity of hydrogen flames towards instabilities.

Two tungsten electrodes were used to ignite the premixed hydrogen/air/EGR mixtures and three ignition energies were applied at the same test condition to determine the minimum spark energy requirement. A Photron-SA5 camera was used to record the flame through two 6 in. quartz windows. A 150 W halogen light source, provided the light for the Z-Schlieren set up equipped with two parabolic mirrors. The frame rate of the camera was adjusted based on the expected flame speed, between 20,000 fps and 75,000 fps with 0.273 mm/pixel resolution. A Kistler 6125C pressure sensor recorded the instantaneous pressure during flame propagation inside the 22.4 liters cylindrical combustion vessel (12 in. both diameter and height). The heated vessel was vacuumed to a pressure less than 1.5 kPa before each test and then washed with dry air twice after the test. The water portion of EGR was injected inside the vessel directly using a high-pressure water injection system. Figure 1 shows a schematic of the current experimental system. More details regarding the instrumentation utilized and the corresponding uncertainty quantification can be found in

[14,18]. The correct mixture composition was achieved by controlling the partial pressure of each of the reactants individually, assuming ideal gas behavior. Based on the stoichiometric global combustion, Equation 1, the partial pressure of the fuel ( $P_{\text{fuel}}$ ) and air ( $P_{\text{air}}$ ) can be calculated based on the air to fuel ratio ( $A_F$ ), the initial pressure ( $P_{\text{initial}}$ ) and the dilution ratio ( $X_{\text{dilution}}$ ), using Equations 2 and 3.

$$H_2 + \frac{1}{2} \left( O_2 + \frac{79}{21} N_2 \right) + \beta H_2 O + Z N_2 \rightarrow$$

$$(1 + \beta) H_2 O + \left( \frac{1}{2} * \frac{79}{21} + Z \right) N_2$$
 (1)

$$P_{\text{fuel}} = \frac{P_{\text{initial}} (1 - X_{\text{dilution}})}{1 + \left(\frac{MW_{\text{fuel}}}{MW_{\text{air}}}\right) * \frac{1}{\phi} * (A_{\text{F}})_{\text{stoic}}}$$
(2)

$$P_{air} = P_{fuel} \left( \frac{MW_{fuel}}{MW_{air}} \right) * \frac{1}{\Phi} * \left( \frac{A}{F} \right)_{stoic}$$
 (3)

The EGR was synthesized from a  $H_2O$  and  $N_2$  mixture to simulate the engine combustion residuals. The partial pressure of the EGR ( $P_{EGR}$ ), EGR  $H_2O$  ( $P_{H_2O}$ ), and EGR  $N_2$  ( $P_{N_2}$ ) in the mixture can be obtained by using Equations 4 to 6.

$$P_{EGR} = P_{initial} X_{dilution}$$
 (4)

$$P_{H_2O} = \frac{\beta}{\beta + Z} P_{EGR} = 0.35 P_{EGR}$$
 (5)

$$P_{N_2} = \frac{Z}{6+Z} P_{EGR} = 0.65 P_{EGR}$$
 (6)

The stoichiometric EGR composition was selected (65%  $N_2$  + 35%  $H_2O$ , by volume) and the dilution ratio, by volume, can be determined using Equation 7.

$$X_{\text{dilution}} = EGR\% = \frac{(\beta+Z)}{1+\frac{1}{2\Phi}(1+\frac{79}{21})+(\beta+Z)}\%$$
 (7)

### 2.2 Laminar burning velocity calculation

An in-house imaging processing code was used to detect and calculate the flame radius, R<sub>f</sub> (t), using the MATLAB canny edge-detection technique. The flame's edge displacement speed, S<sub>b</sub>, is then calculated based on the time derivative of the radius, Equation 8, and it represents the burned gas flame speed. The early flame propagation is affected by the spark energy and the radius data in this region was not used to calculate S<sub>b</sub>, so a lower radius limit of 6-10 mm was used. The maximum radius (R<sub>max</sub>) used to extract the burned gas flame speed, S<sub>b</sub>, is constrained by the radiation and conduction effects, with less effect when the flame volume is less than 25 % of the vessel's volume [14]. Other limitations on R<sub>max</sub> include when the flame begins to experience cellularity, or when buoyancy force affects the flame or pressure builds inside the vessel (>5% P<sub>initial</sub>). Figure 2 shows examples of hydrogen flames affected by buoyancy and cellularity. The propagation speed of the flame edge, calculated in Equation 8, is affected by flame surface

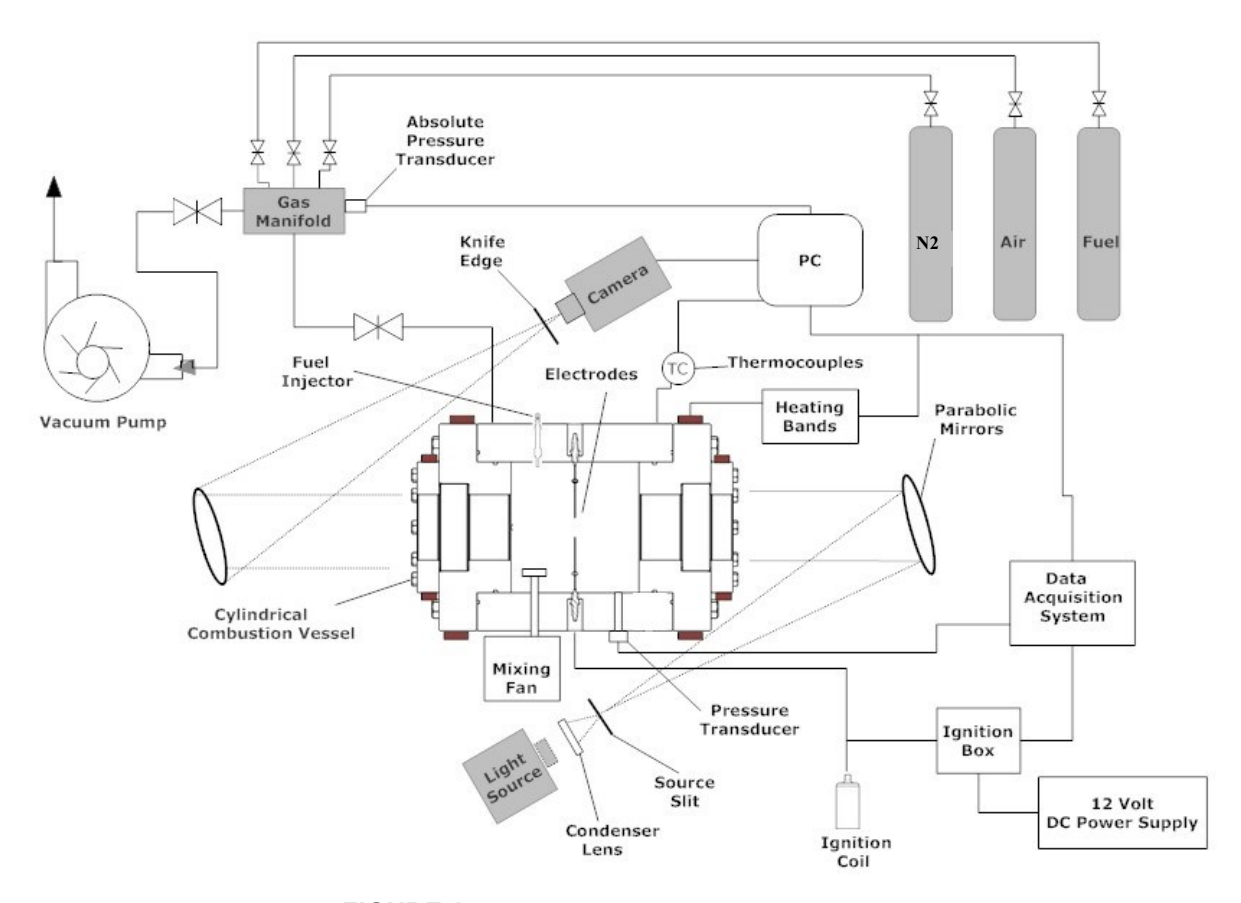


**FIGURE 1:** A schematic of the experimental system [18].

deformation due to flame curvature and strain. Both effects are embodied in the flame stretch ( $\kappa$ ) [28], which is defined for spherical flames in Equation 9. The burned gas flame speed,  $S_b$ , of the measured flames differs significantly from the laminar burning velocity definition due to flame stretch. For expanding spherical flames, the value of stretch is always positive and it decreases with flame development as larger radii flames experience lower stretch levels [28].

$$S_{b} = \frac{dR_{f}}{dt}$$
 (8)

$$\kappa = \frac{1}{A} \frac{dA}{dt} = \frac{2S_b}{R_f}$$
 (9)

The  $\kappa-S_b$  data can be fitted using different correlations and then extrapolated to determine the stretch-free speed [29,30]  $(R_f\to\infty \mbox{ and }\kappa\to 0)$  and the y-intercept of the fitted data curve can be used to define the unstretched value of the burned gas propagation speed,  $S_b^{\ }$ . The curvature-based linear relationship (LC), developed by Markstein [31], was adopted in the  $S_u^{\ }$  calculations, Equation 10. The Markstein length (Lb) includes the effect of curvature, later extended to stretch, on the flame propagation speed.

$$S_b = S_b^{\circ} - S_b^{\circ} \left(\frac{2 L_b}{R_{\epsilon}}\right) \tag{10}$$

It has been reported that the LC method was more accurate for highly stretched flames and mixtures with non-unity Lewis numbers [32,33]. The laminar burning velocity,  $S_u$ °, can be calculated after applying mass continuity through the unstretched flame surface, Equation 11.

$$S_{u}^{\circ} = S_{b}^{\circ} \frac{\rho_{b}}{\rho_{u}} \tag{11}$$

Where,  $\rho$  is the density, and the unburned and burned gases are distinguished by u and b throughout the article.

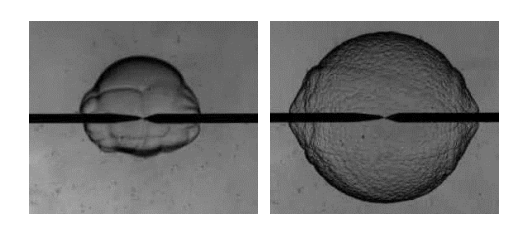


**FIGURE 2:** Hydrogen flame affected by; buoyancy force (left) and hydrodynamic instability (right) at 373 K and 2 bar.

## 2.3 Flame Stability

Lean hydrogen flames tend to be cellular and unstable, during propagation [34] and the severity of wrinkling on the flame

surface is higher at elevated pressures, typical of engine operating conditions [35]. Therefore, prediction of flame cellularity is significant in H2-ICE applications, as the flame can transit from smooth to cellular propagation that eventually can lead to detonation inside the engine [34,36]. The existence of cells on the flame's surface allows for increased reaction zones and this is reflected on the flame propagation speed. The smooth flame propagation can be perturbed hydrodynamic/body forces and by the unbalanced heat and mass diffusions through the flame's surface. The high mass diffusivity of hydrogen and the misalignment of the diffusive and convective fluxes through the spherical flame surface increase the likelihood of cellularity caused by transport properties across the flame (usually called thermo-diffusive instabilities). On the other hand, the thermal expansion, due to the density jump across the flame, can perturb the surface leading to hydrodynamic instabilities.

The change in the flame propagation speed caused by stretch is affected by preferential diffusion, which changes with fuel Lewis number. The balance between heat and mass diffusion away from and into the flame determines the flame response to perturbation and stability at early propagation stages, hence affecting the mixture quenching and ignitability. For flames with positive area deformation (positive stretch), the flame speed will increase with more stretch for mixtures with Le greater than a critical value (Le\*) and vice versa for mixtures with Le <Le\*. Effective Lewis number, Le<sub>eff</sub>, is calculated based on weighted-average fuel and oxidizer Lewis numbers [37], Equation 12. Le<sub>E</sub> represents Lewis number of the excess reactant, air for lean mixture, while Le<sub>D</sub> represents Lewis number of the deficient reactant, fuel for lean mixtures, respectively.

$$Le_{eff} = 1 + \frac{(Le_E - 1) + (Le_D - 1)\xi}{1 + \xi}$$
 (12)

Where,  $\xi$  represents the mixture strength and is positive for rich and lean mixtures  $(\xi = 1 + \text{Ze} (\varphi - 1))$ , and  $\varphi = \frac{1}{\varphi}$  for lean mixtures and  $\varphi = \varphi$  for rich mixtures. Ze is the Zeldovich number and can be calculated using Equation 13 [37].

$$Ze = E \frac{(T_{ad} - T_{u})}{R_{u} T_{ad}^{2}}$$
 (13)

Where E is the global activation energy,  $R_u$  is the universal gas constant,  $T_u$  is the unburned gas temperature and  $T_{ad}$  is the adiabatic flame temperature, calculated from kinetic modelling. On the other hand, the onset and the severity of hydrodynamic instability are affected by the expansion of the burned gases through the flame, which can be quantified by the density jump/ratio across the surface,  $\sigma = \frac{\rho_u}{\rho_b}$ , and by the flame thickness,  $\delta$ . Thinner flames and flames with higher density ratios are more vulnerable to perturbation, and intrinsic hydrodynamic instabilities can be observed at relatively smaller flame radii. Generally, the flame is always affected by

hydrodynamic instabilities, however, this effect is not significant during early flame propagation due to the higher stabilizing stretch effect. The decreasing diffusion transport and stabilizing stretch during flame propagation enhances the hydrodynamic instability and at a critical radius, the sudden appearance of cells dominates the flame surface and a jump in the flame speed is observed. The thermo-diffusive instability for mixtures with Le < Le\* cause large cracks to form on the surface and this effect is mitigated at larger radii due to the reduced diffusion transport effect.

Flame thickness can be calculated using several expressions [38]. Xie et al. [39] compared three correlations to calculate the flame thickness and recommended considering both the hydrogen diffusion effect and the non-inert preheat zone in the calculation of flame thickness. The modified flame thickness can be calculated using Equation 14, and it was observed that the flame thickness increased after considering the H-atom diffusion into the preheat zone [39].

$$\delta = \frac{\left(\frac{K}{Cp}\right)_{T_0}}{\left(\rho_u \, S_u^{\circ}\right)} \tag{14}$$

Where, the ratio of thermal conductivity (K) to specific heat (Cp) was calculated at an inner-layer temperature derived from [40] for hydrogen fuel.

## 2.4 Modeling Details

Kinetic modeling was used to further investigate the effect of dilution on the laminar burning velocity. The XJTUNO-2021 mechanism [22], which was based on the mechanism developed by [41], was adopted. The mechanism contains 44 species and 266 elementary reactions with updated NOx chemistry. Chemkin-Pro [42] 1-D simulations of the planar flame propagation were performed and the results were validated with the experimental data.

### 3 RESULTS AND DISCUSSIONS

## 3.1 Laminar burning velocity results

Mixtures of H<sub>2</sub>/air were ignited at a pressure of 2 bar and different EGR dilution ratios, up to 50% by volume. All the tests were conducted at initial temperature of 373 K. Furthermore, the equivalence ratio was changed from stoichiometric ( $\phi = 1.0$ ) to ( $\phi = 0.7$ ) to study mixture strength effect. The properties of the tested mixtures were calculated using Chemkin-Pro [42] and are listed in Table 1, where  $\gamma$ ,  $\sigma$ and  $\alpha$  are the specific heat ratio, the density ratio and the mixture thermal diffusivity, respectively. Figure 3 shows the burned gas flame speed, S<sub>b</sub>, vs. flame radius for both experimental and the LC model results at 2 bar, 373 K and 40 % EGR. The effect of the spark energy on the early flame propagation can be observed at small flame radii. This sparkaffected data deviates from the stable flame propagation data and therefore it was excluded from the data-fitting for better estimation of S<sub>u</sub>°. The experimental data also deviated from the model at the onset of the flame instabilities when the flame began to accelerate, indicated by a rise in S<sub>b</sub>, due to the increase of surface area. The graph highlights the significance of the

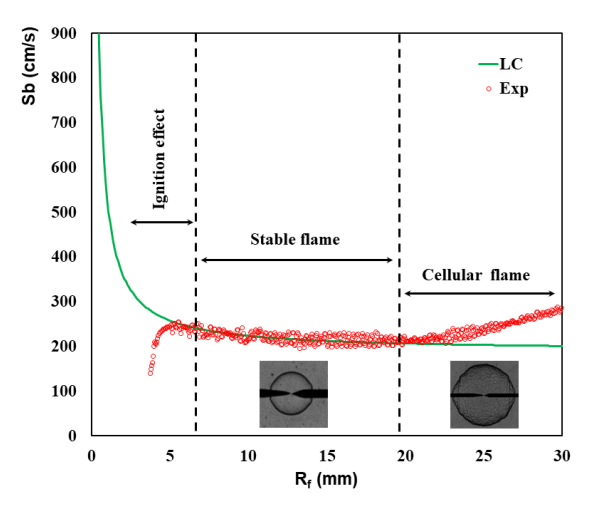
selection of the stable-flame data for the  $S_b - \kappa$  fitting and the calculation of  $S_u$ °. Figure 4 shows the stretched burned gas flame speeds of the hydrogen flames vs. the flame radius at different dilution ratios at 2 bar, 373 K, and stoichiometric conditions. Generally, a reduction in  $S_b$  values with dilution can be observed from the graph. For all dilution ratios, the flame speed was affected by the ignition event at small radii. The radius at which this effect is minimal was determined independently for each test condition.

Table 1: Properties and test conditions of the experiments.

P	T	ф	EGR	γ	σ	T <sub>ad</sub>	α	Le <sub>eff</sub>
[bar]	K	[-]	[%]	[-]	[-]	(K)	$[10^{-5}\text{m}^2/\text{s}]$	[-]
2	373	0.7	0	1.3957	4.93	2074	2.968	0.56
			10	1.3928	4.59	1908	2.821	0.54
			20	1.3899	4.24	1738	2.677	0.51
			30	1.3870	3.87	1569	2.536	0.49
			40	1.3842	3.50	1400	2.396	0.45
2	373	1.0	0	1.3959	5.63	2441	3.386	1.10
			10	1.3929	5.33	2280	3.192	1.06
			20	1.3900	4.97	2098	3.002	1.01
			30	1.3871	4.56	1897	2.816	0.97
			40	1.3843	4.12	1687	2.633	0.92
			50	1.3815	3.66	1474	2.454	0.88

The flame propagated in a stable or smooth mode, bounded by the ignition affected propagation and the cellularity onset point. However, the stretch effect on the burned gas flame speeds of those smooth flames varied with dilution. Positive slopes for the  $S_b-R_f$  curves were observed for dilution  $\leq 20\%$ , indicating a negative stretch-speed effect, as shown in Figure 5. On the other hand, negative slopes of  $S_b-R_f$  curves, indicating positive stretch-speed dependence, were observed at 30%, 40%, and 50% EGR. For all dilution ratios, the linear dependence of  $S_b-\kappa$  was not maintained when the cellularity began to disturb the flame surface and that cellular modulation altered the  $S_b-\kappa$  interaction.

Figure 6 illustrates the flame speed versus stretch for leaner hydrogen/air mixtures at ( $\phi$  =0.7), 2 bar and 373 K. For all EGR ratios, positive S<sub>b</sub> response to stretch was observed and the flame speed decreased during the smooth non-cellular flame propagation with increasing flame radius and decreasing stretch. In all cases, increasing the dilution ratio increased the slope of the  $S_b - \kappa$  curve and the effect of stretch on the flame speed was increased. The laminar burning velocity, Su, was calculated using Equation 11 for all test conditions. Three tests were repeated at each condition and the average S<sub>u</sub> values were calculated. A comparison of the laminar burning velocities of hydrogen/air flames at different dilution ratios at  $\phi$ = 1.0 and  $\phi$ = 0.7 is shown in Figure 7. It can be seen in Figure 7 that the laminar burning velocity decreases with increasing dilution. For stoichiometric mixtures at 2 bar and 373 K, adding 10% EGR to the mixture decreased  $S_u^{\circ}$  from to 309 cm/s to 238 cm/s, a



**FIGURE 3:** Comparison between the LC model and the experimental data, showing ignition, smooth and unstable regions at 373K, 2 bar, 40% EGR and stoichiometric H<sub>2</sub>/air mixture.

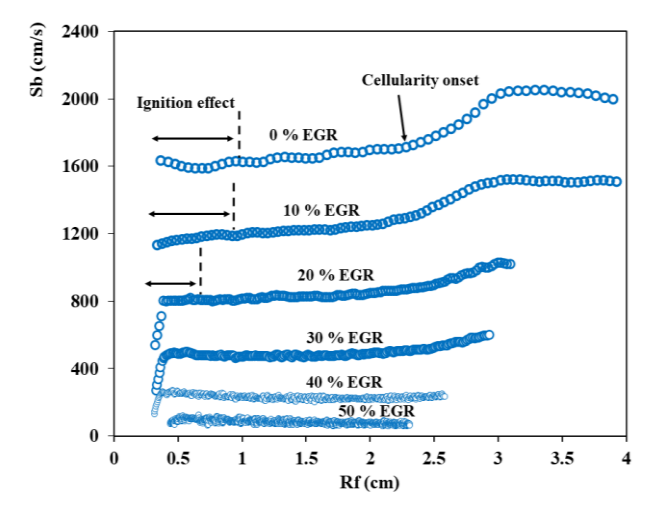


**FIGURE 4:** Stretched flame speed versus flame radius at different EGR ratios at 2 bar, 373K, and  $\phi = 1.0$ .

reduction of 23%. Further increasing the dilution from 10% to 20%, 30%, 40% and 50% changed  $S_u^{\ }$  to 185 cm/s, 103 cm/s, 48 cm/s and 17 cm/s, respectively. The reduction percentages of  $S_u^{\ }$  with dilution, relative to the non-diluted value ( $S_u^{\ }=309$  cm/s @ 0% EGR) are 45%, 67%, 85% and 94% at 20%, 30%, 40% and 50% EGR, respectively. Figure 7 also illustrates the results for lean hydrogen/air mixtures at  $\varphi=0.7$ . A similar trend can be seen with EGR addition.  $S_u^{\ }$  measured values at 0%, 10%, 20%, 30% and 40% EGR, were 173.1 cm/s, 121.7 cm/s, 77.3 cm/s, 42.1 cm/s and 16.1 cm/s, respectively at  $\varphi=0.7$ . The percentage decreased of  $S_u^{\ }$  at each EGR ratio, relative to  $S_u^{\ }$  at 0% EGR (173 cm/s) was 30%, 55%, 76% and 91% when the EGR was increased by 10%, 20%, 30% and 40%, respectively. Measurements of  $S_u^{\ }$  at 50% EGR and  $\varphi=0.7$  were not possible

due the buoyancy effect on the flame. The leaner mixtures experienced lower flame burning velocities compared to the stoichiometric mixtures. The percentage decrease in  $S_u^{\ \ }$  from  $\varphi=1$  to  $\varphi=0.7$  was 44%, 48.9%, 56.3% and 58.9% at 10%, 20%, 30% and 40% EGR, respectively. Numerical results of  $S_u^{\ \ }$  calculated with Chemkin-Pro were compared with the experimental results, refer to Figure 7. The mechanism agreed well with the experimental results with a RMSE of 2.8 cm/s and 3.7 cm/s at  $\varphi=0.7$  and  $\varphi=1.0$ , respectively. The decrease in  $S_u^{\ \ \ }$  with additional EGR indicates a reduction in the mixture reactivity and exothermicity, as the adiabatic flame temperature decreased with EGR dilution, as listed in Table 1.

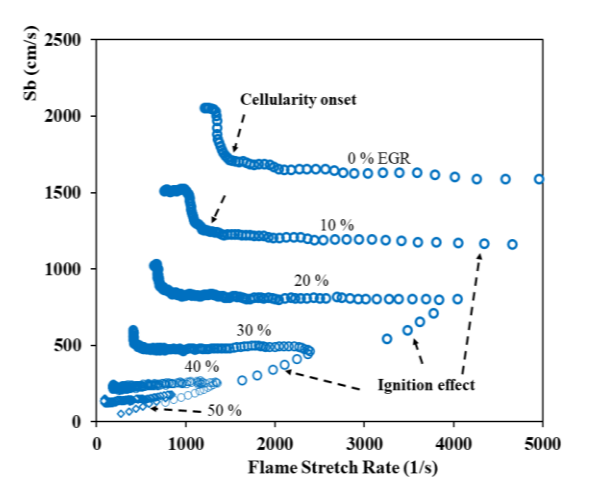


**FIGURE 5:** Flame speed-stretch curves at 2 bar, 373 K and  $\phi$ =1.0. and 0% to 50% dilution.

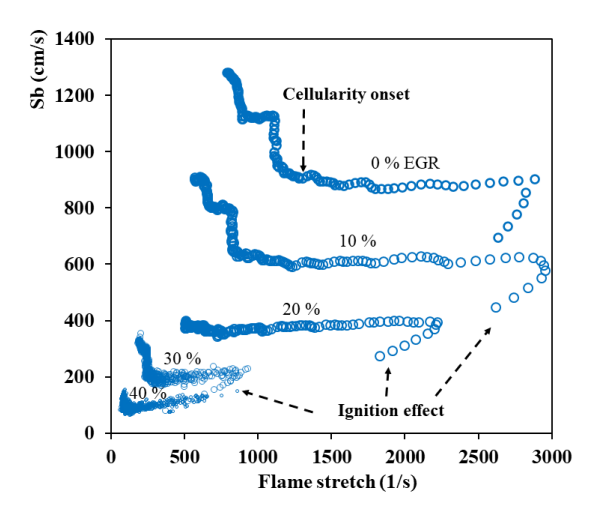


**FIGURE 6:** Flame speed-stretch curves at 2 bar, 373 K,  $\phi$ =0.7. and 0% to 50% dilution.

The reduction of the flame temperature suppressed the chain branching reactions, temperature sensitive, and reduced the O, H and OH pool [43]. The mixture reactivity can be correlated with the hydroxyl (OH) radical pool in the reaction zone, as OH participates in the chain branching reactions which accelerates the flame. The OH radical also participates in the formation of NOx and affects the flame structure. Figure 8 shows the peak OH mole fraction for each of the diluted flames, calculated from kinetic modeling of 1-D freely propagating flames at the

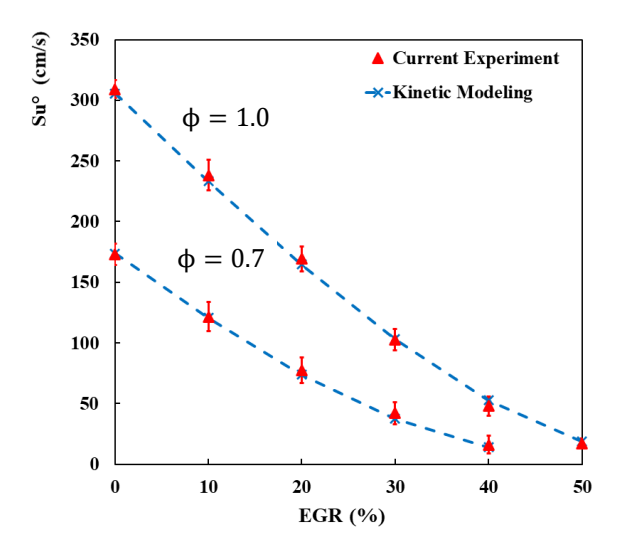


**FIGURE 7:** Laminar burning velocity at different levels of EGR dilution at 373 K and 2 bar.

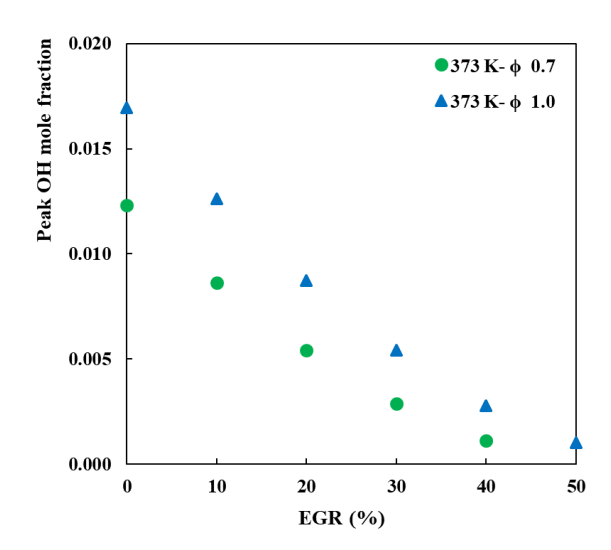


**FIGURE 8:** Peak OH mole fraction versus EGR at 2 bar.

corresponding conditions. The OH concentration decreased dramatically with increasing EGR and decreasing equivalence ratio, indicating lower reactivity. The trend of OH reduction, shown in Figure 8, can be correlated to the reduction in  $S_u$  presented in Figure 7, similar observations were made by [17,43,44]. Figure 9 shows the maximum parts per million per volume dry (Ppmvd) of NOx versus dilution ratios at 2 bar, 373 K and  $\varphi = 1.0$  and  $\varphi = 0.7$ , extracted from kinetic modelling.

The suppression of thermal NOx formation by reducing the combustion temperature is confirmed from the plot in Figure 9. Diluting the stoichiometric mixture by 10 % EGR reduced NOx max Ppmvd by 80% compared to its value at 0% EGR. A reduction of 87%, 86%, 72%, 72 % was obtained at 20%, 30, 40% and 50% EGR, respectively. At  $\varphi$  = 0.7, Max NOx Ppmvd decreased by 89% by at 10% EGR compared to non-diluted mixture max NOx. This reduction of max Ppmvd NOx can be attributed to reduced OH mole fraction with dilution, Figure 8, and the lower adiabatic flame temperature of diluted mixtures at higher EGR concentrations, Table 1.

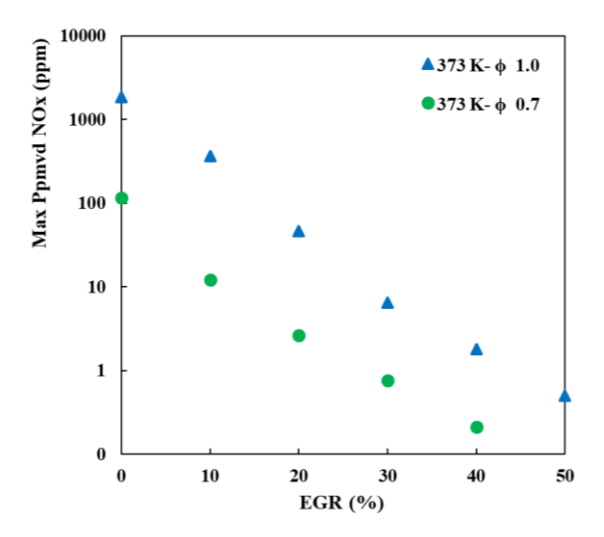


**FIGURE 9:** Maximum Ppmvd of NOx versus EGR dilution at 2 bar and 373 K.

# 3.2 Flame Morphology and stability

Many modern premixed combustion systems rely on lean burn and/or EGR dilution to improve the efficiency and meet NOx standards [3]. The effect of the diluents on the flame stability and morphology impacts combustion and, consequently, the engine operating range. The experimental results indicate that the early flame propagation was smooth, even for highly diluted flames. From Figure 10, it can be seen that following the initial smooth flame, large wrinkles begin to form until a point where the entire flame surface becomes cellular and the surface can be characterized by small cells and wrinkles. Flame destabilization is increased by three mechanisms: thermo-diffusive, hydrodynamic, and body forces. In this section, the flame instabilities and surface morphology are investigated at different EGR ratios. In Figure 10, Schlieren images of the detected flames at different dilution ratios at 373 K and 2 bar are shown at different times and radii. It was observed that the curvature and stretch are a stabilizing mechanism of the stretched flames and that this effect is significant at smaller flame radii as curvature weakens with the increases in the flame size. The thermo-diffusive instability is only significant for mixtures of unbalanced heat and mass diffusivities, characterized by a Lewis number less than Le\*, near unity. Hydrodynamic instability is caused by thermal expansion

through the flame surface due to the transition from cold to hot gases (sometimes called Darrius-Luanda (DL) instability). This always affects the flame due to the intrinsic densitydiscontinuity at the flame surface all the time. Lastly, the buoyancy or body force is important for relatively slow flames. The combined effect of the aforementioned stabilization/destabilization mechanisms determines the point (critical radius) when the surface is fully wrinkled and a cellular flame can be distinguished. To quantitively identify each mechanism separately, the Lewis number, density ratio and flame thickness were calculated using kinetic modeling. The thermodiffusive instability can be predicted by calculating the Lewis number for each diluted mixture. The Lewis number values, listed in Table 1, are also plotted in Figure 11 versus EGR ratio. Mixtures at 373 K, 2 bar,  $\phi = 1.0$ , and 0%, 10% and 20% EGR ratios exhibited  $Le_{eff} > 1.0$ . In these cases, thermal diffusion was balanced with mass diffusion into the flame and hence a stable flame in terms of themodiffusional instabilities was obtained. Increasing the dilution above 30% decreases the Leeff and therefore the flame tendency toward thermo-diffusive instability increases. For lean mixtures,  $\phi = 0.7$  at 337 K and 2 bar, a Le<sub>eff</sub> < 0.6 was observed and the Le<sub>eff</sub> decreased with EGR, indicating that there was a greater effect from thermodiffusive instabilities on these flames. However, the stabilizing effect of curvature at small radii overrides the thermo-diffusive instability and it smooths the flame surface at small radii, as shown in Figure 10 (a), (b), and (c) at  $R_f < 2.0$  cm. Hydrodynamic instability is enhanced by reducing the flame thickness and increasing the density ratio across the flame. In this regard, Figures 12 and 13 show the calculated flame thickness and density ratios, respectively, for different levels of EGR dilution. Flame thickness increases with dilution due to lower mixture reactivity and slower flame speeds. Greater flame thickness can inhibit disturbances on the flame surface. Moreover, the jump in the density across the flame surface decreases with increasing EGR. The combined effect of the higher flame thickness and the smaller density jump decreases the thermal expansion across the flame and dampens low wavelength disturbances by gas motion that can destabilize the flame hydrodynamically.

Hence, the flame resistance to hydrodynamic instability increases with dilution. This effect is enhanced further for the lean mixture,  $\phi = 0.7$ , due to the excess air, as shown in Figures 12 and 13. A competing effect of the decreased Lewis number (increased thermodiffusive instabilities) and the decreased thermal expansion (mitigated hydrodynamic instabilities) determines the onset of cellularity of the flame with EGR. Figure 14 shows the critical radius related to the onset of cellularity at different conditions. For stoichiometric mixtures, increasing EGR up to 20% decreases the critical radius and the increased thermodiffusive instabilities surpass the reduced DL instabilities. At EGR > 30%, the critical radius increases with dilution due to the mitigating effect of hydrodynamic instability associated with reduced thermal expansion through the flame. Leaner mixtures ( $\phi = 0.7$ ) start to become cellular at smaller radii, relative to stoichiometric mixtures. The inflection-point

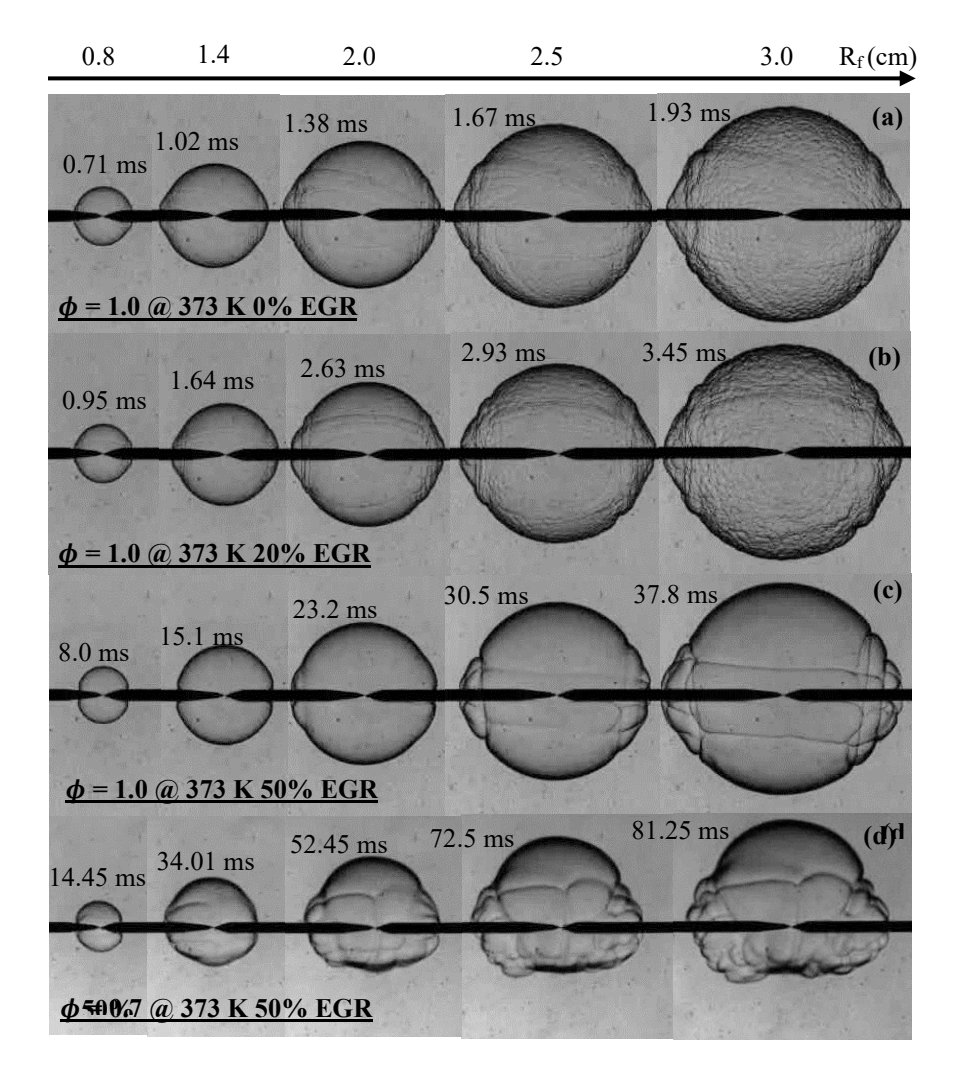


**FIGURE 10:** Schlieren images of the flame morphology versus time at 2 bar and 373 K.

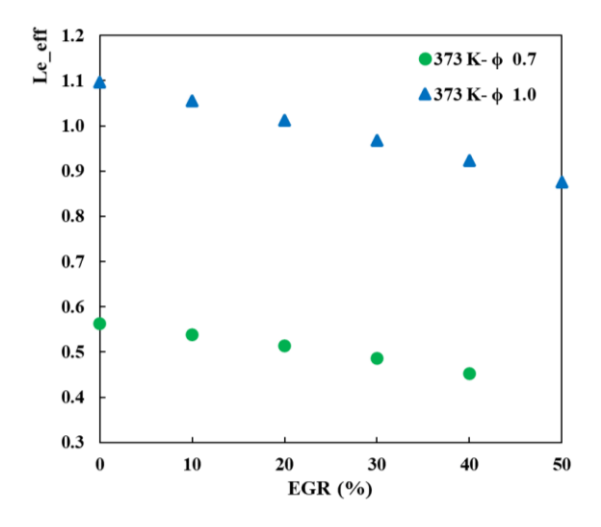


**FIGURE 11:** Effective Lewis number versus EGR dilution at 2 bar and 373 K.

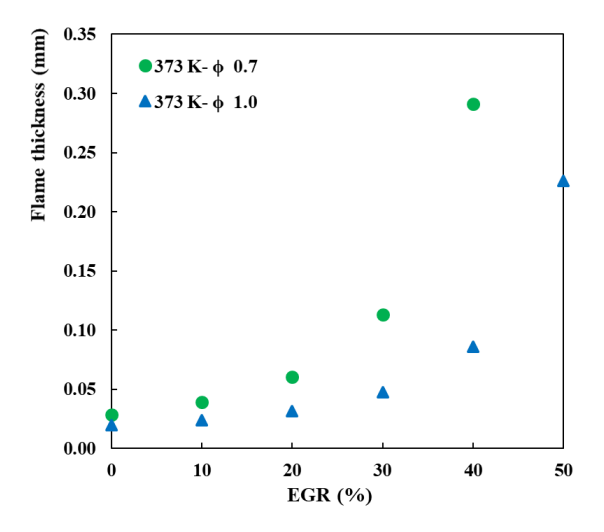


**FIGURE 12:** Flame thickness versus EGR dilution at 2 bar and 373 K.

of the  $R_{cr}$  – EGR curve of  $\varphi=0.7$  is at 20% EGR, which is earlier than the 30% point for stoichiometric mixtures. This can be attributed to the reduction of thermal expansion in leaner mixtures. While higher EGR ratios dampen flame hydrodynamic instabilities, they can lead to other combustion instabilities, such as misfire and flame quenching. It is worth mentioning that the calculated values of the flame thickness, based on Equation 14 and  $(\frac{K}{Cp})$  calculated at an inner layer temperature  $T_0$ , is relatively larger than the values predicted in [39]. Nevertheless,  $\delta$  shown in Figure 12 is still following the same increasing trend with EGR. Burned gas Markstein length  $(L_h)$  is used to quantify the sensitivity of the flame speed to the

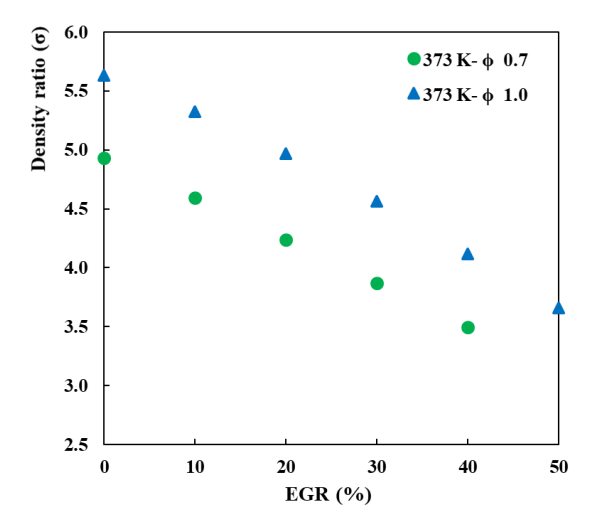


**FIGURE 13:** Density ratio across the flame versus EGR dilution at 2 bar and 373 K.

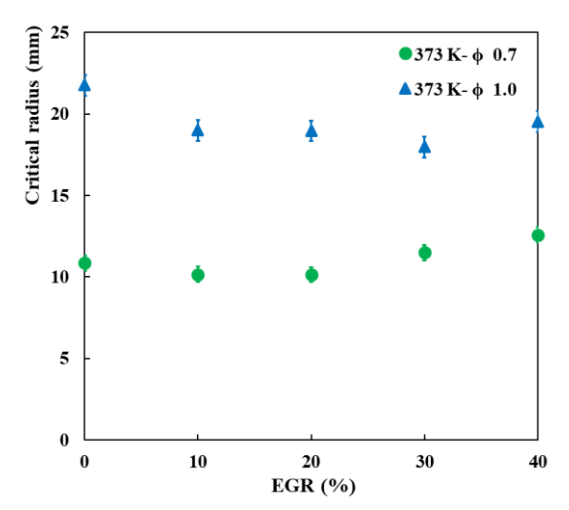


**FIGURE 14:** Critical radius versus EGR dilution at 2 bar and 373 K.

local curvature and strain.  $L_b$  is derived from the slope of the speed-stretch curve, based on Equation 10 and is shown in Figure 15. Positive  $L_b$  at EGR  $\leq$  20 % at 373 K, 2 bar and  $\varphi$  =

1.0, indicates a negative or decreased stretched flame speed, indicated by the negative slope in Figures 4 and 5. The reduction in flame speed with stretch tends to stabilize the flame, as cell formation stretches the flame and the decreased speed helps to dampen any surface disturbance. For all other mixtures, negative values of  $L_b$  were observed. For  $L_b < 0$ , the stretch has a positive effect and stretched flame speeds accelerate while propagating in the smooth-surface regime. The flame response to stretch is significant in practical premixed systems as the flame is highly stretched and turbulent and stretch can accelerate or decelerate the flame. The buoyancy force affected the stoichiometric flame at 50% EGR and larger radii, and this effect was enhanced at  $\Phi = 0.7$ .

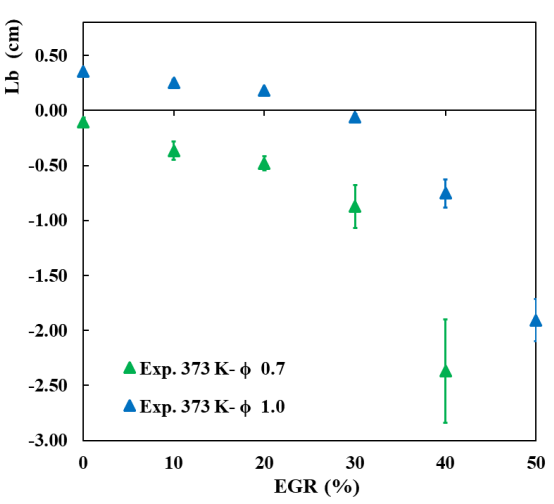


**FIGURE 15:** Markstein length versus EGR dilution at 2 bar and 373 K.

The slower flame associated with the 50% dilution ratio allowed the buoyancy force to disturb the flame surface and the flame was lifted up with time, as shown in Figure 10 (c) and (d), where the flame geometrical center can be seen to move upward relative to the ignition point. It is worth mentioning that at engine relevant conditions (higher pressures and temperatures), the effect of the increased flame speed due to the higher temperatures is counteracted by the decreased flame speed at higher pressures, which gives significance to the current data conducted at relatively lower pressure.

## 4 CONCLUSIONS

Diluted hydrogen/air mixtures were ignited inside a constant volume vessel at 2 bar and 373 K at mixture strengths of  $\varphi = 1.0$  and  $\varphi = 0.7$ , and varying levels of EGR dilution. Actual composition of EGR (35% H<sub>2</sub>O+65%N<sub>2</sub>, by volume) was used at ratios of 0% to 50%, by volume. Kinetic modeling was performed using ANSYS Chemkin-Pro software at the corresponding conditions. The primary objective was to investigate the impact of EGR on laminar burning velocity and flame stability as significant parameters in the context of hydrogen internal combustion engines (H2-ICE). Simulation results of the laminar burning velocity were validated with the

experimental measurements and showed a good agreement. Increasing dilution ratio decreased the laminar burning velocity in all cases and more reduction was observed at higher EGR ratios (> 20%). This observation was confirmed by the reduction in the maximum OH mole fraction in the reaction zone.

Flame stability response to EGR showed a decrease in the critical radius, representing the onset of cellularity, with EGR up to a specific threshold (20% to 30% EGR). Beyond this value, further increase in EGR increased the critical radius and stabilized the flame. The flame thickness and density jump were confirmed with the schlieren images and OH mole fractions indicating the lower reactivity of the diluted flames. Lastly, the addition of EGR, above a threshold, increased the hydrodynamic stability margin of the flames.

#### **ACKNOWLEDGEMENTS**

This material is based upon work supported by the National Science Foundation under Grant No. 2129229. The authors would also like to thank the Joseph M. and Suzanne H. Colucci Endowed Graduate Fellowship.

### **REFERENCES**

- Use of Oil U.S. Energy Information Administration (EIA) n.d. https://www.eia.gov/energyexplained/oil-and-petroleum-products/useof-oil.php (accessed April 24, 2024).
- Wind-to-Hydrogen Project | Hydrogen and Fuel Cells | NREL n.d. <a href="https://www.nrel.gov/hydrogen/wind-to-hydrogen.html">https://www.nrel.gov/hydrogen/wind-to-hydrogen.html</a> (accessed January 20, 2023).
- [3] Wang S, Zhai Y, Wang Z, Hou R, Zhang T, Ji C. Comparison of Air and EGR with Different Water Fractions Dilutions on the Combustion of Hydrogen-Air Mixtures 2022. https://doi.org/10.1016/j.fuel.2022.124686.
- [4] Ge H, Bakir AH, Zhao P. Knock Mitigation and Power Enhancement of Hydrogen Spark-Ignition Engine through Ammonia Blending. Machines 2023, Vol 11, Page 651 2023;11:651. https://doi.org/10.3390/machines11060651.
- [5] Shaffer J, Alvarez LF, Askari O. Investigation of High-Pressure Laminar Flame Speed Measurement. ASME International Mechanical Engineering Congress and Exposition, Proceedings (IMECE) 2024;10. https://doi.org/10.1115/IMECE2023-113441.
- [6] Alvarez LF, Shaffer J, Dumitrescu CE, Askari O. Laminar Burning Velocity of Ammonia/Air Mixtures at High Pressures. Fuel 2024;363:130986. https://doi.org/10.1016/J.fuel.2024.130986.
- [7] Boretti A. Hydrogen Internal Combustion Engines to 2030 2020. https://doi.org/10.1016/j.ijhydene.2020.06.022.
- [8] Ingo C, Tuuf J, Björklund-Sänkiaho M. Experimental Study of the Performance of a SI-Engine Fueled with Hydrogen-Natural Gas Mixtures. Int J Hydrogen Energy 2024;63:1036–43. https://doi.org/10.1016/J.IJHYDENE.2024.03.252.
- [9] Inbanaathan PV, Balasubramanian D, Nguyen VN, Le VV, Wae-Hayee M, R R, et al. Comprehensive Study On Using Hydrogen-Gasoline-Ethanol Blends as Flexible Fuels in an Existing Variable Speed SI Engine. Int J Hydrogen Energy 2023;48:39531–52. https://doi.org/10.1016/J.ijhydene.2023.03.107.
- [10] Suresh D, Porpatham E. Influence of High Compression Ratio and Hydrogen Addition on the Performance and Emissions of a Lean Burn Spark Ignition Engine Fueled by Ethanol-Gasoline. Int J Hydrogen Energy 2023;48:14433–48. https://doi.org/10.1016/J.ijhydene.2022.12.275.
- [11] Verhelst S, Wallner T. Hydrogen-Fueled Internal Combustion Engines. Prog Energy Combust Sci 2009;35:490–527. https://doi.org/10.1016/j.pecs.2009.08.001.

- [12] Özyalcin C, Sterlepper S, Roiser S, Eichlseder H, Pischinger S. Exhaust Gas Aftertreatment to Minimize NOx Emissions from Hydrogen-Fueled Internal Combustion Engines. Appl Energy 2024;353:122045. https://doi.org/10.1016/J.apenergy.2023.122045.
- [13] Dhyani V, Subramanian KA. Control of Backfire and NOx Emission Reduction in a Hydrogen Fueled Multi-Cylinder Spark Ignition Engine Using Cooled EGR and Water Injection Strategies. Int J Hydrogen Energy 2019;44:6287–98. https://doi.org/10.1016/J.IJHYDENE.2019.01.129.
- [14] Duva BC, Toulson E. Unstretched Unburned Flame Speed and Burned Gas Markstein Length of Diluted Hydrogen/Air Mixtures. Int J Hydrogen Energy 2022;47:9030–44. https://doi.org/10.1016/J.ijhydene.2021.12.217.
- [15] Rrustemi DN, Ganippa LC, Megaritis T, Axon CJ. New Laminar Flame Speed Correlation for Lean Mixtures of Hydrogen Combustion with Water Addition under High Pressure Conditions. Int J Hydrogen Energy 2024;63:609–17. https://doi.org/10.1016/J.ijhydene.2024.03.177.
- [16] Verhelst S, Woolley R, Lawes M, Sierens R. Laminar and Unstable Burning Velocities and Markstein Lengths of Hydrogen—Air Mixtures at Engine-Like CONDITIONS. Proceedings of the Combustion Institute 2005;30:209–16. https://doi.org/10.1016/J.proci.2004.07.042.
- [17] Kwon OC, Faeth GM. Flame/Stretch Interactions of Premixed Hydrogen-Fueled Flames: Measurements and Predictions. Combust Flame 2001;124:590–610. <a href="https://doi.org/10.1016/S0010-2180(00)00229-7">https://doi.org/10.1016/S0010-2180(00)00229-7</a>.
- [18] Barain A, Trombley G, Duva BC, Toulson E. Laminar Burning Velocities of Diluted Stoichiometric Hydrogen/Air Mixtures. SAE Technical Papers 2023. <u>https://doi.org/10.4271/2023-01-0331</u>.
- [19] Lamoureux N, Djebaïli-Chaumeix N, Paillard CE. Laminar Flame Velocity Determination for H2-air-He-CO2 Mixtures using the Spherical Bomb Method. Exp Therm Fluid Sci 2003;27:385-93. https://doi.org/10.1016/S0894-1777(02)00243-1.
- [20] Duva BC, Chance LE, Toulson E. Dilution Effect of Different Combustion Residuals on Laminar Burning Velocities and Burned Gas Markstein Lengths of Premixed Methane/Air Mixtures at Elevated Temperature. Fuel 2020;267:117153. https://doi.org/10.1016/J.fuel.2020.117153.
- [21] Sabdenov KO. Effect of Molar Mass Variation on a Flame Temperature and a Burning Rate. Combust Explos Shock Waves 2021;57:46–52. https://doi.org/10.1134/S0010508221010056/figures/2.
- [22] Sun W, Zhao Q, Curran HJ, Deng F, Zhao N, Zheng H, et al. Further Insights into the Core Mechanism of H2/CO/NOx Reaction System. Combust Flame 2022;245:112308. https://doi.org/10.1016/J.combustflame.2022.112308.
- [23] Duva BC, Chance L, Toulson E. Laminar Flame Speeds of Premixed Iso-Octane/Air Flames at High Temperatures with CO<sub>2</sub> Dilution. SAE Int J Adv Curr Pract Mobil 2019;1:1148–57. https://doi.org/10.4271/2019-01-0572.
- [24] Alvarez LF, Shaffer J, Dumitrescu C, Askari O. Investigation of NH3/Air Laminar Burning Speed and Flame Structure at High Pressures. ASME International Mechanical Engineering Congress and Exposition, Proceedings (IMECE) 2024;10. https://doi.org/10.1115/IMECE2023-112269.
- [25] Duva BC. Investigation of the Dilution Effect on Laminar Flame Characteristics in a Constant Volume Combustion Chamber. Michigan State University; 2021. Doctoral Thesis.
- [26] Rokni E, Moghaddas A, Omid A, Metghalchi H. Measurement of Laminar Burning Speeds and Investigation of Flame Stability of Acetylene (C2H2)/Air Mixtures. Journal of Energy Resources Technology, Transactions of the ASME 2015;137. https://doi.org/10.1115/1.4028363/443344.
- [27] Xiouris C, Ye T, Jayachandran J, Egolfopoulos FN. Laminar Flame Speeds under Engine-Relevant Conditions: Uncertainty quantification and minimization in spherically expanding flame experiments. Combust Flame 2015;163:270–83. https://doi.org/10.1016/j.combustflame.2015.10.003.
- [28] Chen Z. On the Extraction of Laminar Flame Speed and Markstein length from Outwardly Propagating Spherical Flames. Combust Flame 2011;158:291–300. https://doi.org/10.1016/J.combustflame.2010.09.001.

- [29] Wu CK, Law CK. On the Determination of Laminar Flame Speeds from Stretched Flames. Symposium (International) on Combustion 1985;20:1941–9. https://doi.org/10.1016/S0082-0784(85)80693-7.
- [30] Matalon M. On Flame Stretch. Combustion Science and Technology 1983;31:169–81. https://doi.org/10.1080/00102208308923638.
- [31] MARKSTEIN GH. Experimental and Theoretical Studies of Flame-Front Stability. Dynamics of Curved Fronts 1988:413–23. https://doi.org/10.1016/B978-0-08-092523-3.50045-9.
- [32] Shaffer J, Askari O. Measurement of Laminar Burning Speed at High Pressures using Plasma Affected Flame. Combust Flame 2024;263:113402. <a href="https://doi.org/10.1016/J.combustflame.2024.113402">https://doi.org/10.1016/J.combustflame.2024.113402</a>.
- [33] Giannakopoulos GK, Gatzoulis A, Frouzakis CE, Matalon M, Tomboulides AG. Consistent Definitions of Flame Displacement Speed" and Markstein Length for Premixed Flame Propagation. Combust Flame 2015;162:1249–64. https://doi.org/10.1016/J.combustflame.2014.10.015.
- [34] Bechtold JK, Matalon M. Hydrodynamic and Diffusion Effects on the Stability of Spherically Expanding Flames. Combust Flame 1987;67:77–90.
- [35] Manton J, Guenther Von Elbe; Lewis B. Nonisotropic Propagation of Combustion Waves in Explosive Gas Mixtures and the Development of Cellular Flames. J Chem Phys 1952;20:153–7. https://doi.org/10.1063/1.1700159.
- [36] Liu Q, Chen X, Shen Y, Zhang Y. Parameter Extraction from Spherically Expanding Flames Propagated in Hydrogen/Air Mixtures 2018. https://doi.org/10.1016/j.ijhydene.2018.11.004.
- [37] Wang LQ, Ge Y, Ma HH. Revisiting Effective Lewis Number of Combustible Mixtures. Fuel 2023;343:127909. https://doi.org/10.1016/J.fuel.2023.127909.
- [38] Bradley D, Lawes M, Mansour MS. Explosion Bomb Measurements of Ethanol–Air Laminar Gaseous Flame Characteristics at Pressures up to 1.4 MPa. Combust Flame 2009;156:1462–70. https://doi.org/10.1016/J.combustflame.2009.02.007.
- [39] Xie Y, Elsayed Morsy M, Li J, Yang J. Intrinsic Cellular Instabilities of Hydrogen Laminar Outwardly Propagating Spherical Flames. Fuel 2022;327:125149. https://doi.org/10.1016/J.FUEL.2022.125149.
- [40] Flames P, Goti'gens J, Mauss F, Peters N. Analytic Approximations of Burning Velocities and Flame Thicknesses of Lean Hydrogen 1992:129–35.
- [41] Kéromnès A, Metcalfe WK, Heufer KA, Donohoe N, Das AK, Sung CJ, et al. An Experimental and Detailed Chemical Kinetic Modeling Study of Hydrogen and Syngas Mixture Oxidation at Elevated Pressures. Combust Flame 2013;160:995–1011. https://doi.org/10.1016/J.combustflame.2013.01.001.
- [42] Ansys Chemkin-Pro | Chemical Kinetics Simulation Software n.d. https://www.ansys.com/products/fluids/ansys-chemkin-pro (accessed May 2, 2024).
- [43] Hu E, Huang Z, He J, Miao H. Experimental and Numerical Study on Lean Premixed Methane–Hydrogen–Air flames at elevated pressures and temperatures. Int J Hydrogen Energy 2009;34:6951–60. https://doi.org/10.1016/J.IJHYDENE.2009.06.072.
- [44] Zhang X, Wang J, Chen Y, Li C. Effect of CH4, Pressure, and Initial Temperature on the Laminar Flame Speed of an NH3-Air Mixture. ACS Omega 2021;6:11857–68. https://doi.org/10.1021/ACSOMEGA.1C00080.